

A DATA-DEPENDENT REGULARIZATION METHOD BASED ON THE GRAPH LAPLACIAN

DAVIDE BIANCHI*, DAVIDE EVANGELISTA†, STEFANO ALEOTTI‡, MARCO DONATELLI‡, ELENA LOLI PICCOLOMINI†, AND WENBIN LI§

Abstract. We investigate a variational method for ill-posed problems, named **graphLa+Ψ**, which embeds a graph Laplacian operator in the regularization term. The novelty of this method lies in constructing the graph Laplacian based on a preliminary approximation of the solution, which is obtained using any existing reconstruction method Ψ from the literature. As a result, the regularization term is both dependent on and adaptive to the observed data and noise. We demonstrate that **graphLa+Ψ** is a regularization method and rigorously establish both its convergence and stability properties.

We present selected numerical experiments in 2D computerized tomography, wherein we integrate the **graphLa+Ψ** method with various reconstruction techniques Ψ , including Filter Back Projection (**graphLa+FBP**), standard Tikhonov (**graphLa+Tik**), Total Variation (**graphLa+TV**), and a trained deep neural network (**graphLa+Net**). The **graphLa+Ψ** approach significantly enhances the quality of the approximated solutions for each method Ψ . Notably, **graphLa+Net** is outperforming, offering a robust and stable application of deep neural networks in solving inverse problems.

Key words. ill-posed problems; non-local operators; graph Laplacian; deep learning; deep neural networks; medical imaging

MSC codes. 47A52; 05C90; 68T07; 92C55

1. Introduction.

We consider the model equation

$$(ME) \quad Kx = y^\delta,$$

where $K: X \simeq \mathbb{R}^n \rightarrow Y \simeq \mathbb{R}^m$ represents a discretized version of a linear operator that is inherently ill-posed. Given a fixed $x_{gt} \in X$ and $y := Kx_{gt}$, we want to recover a good approximation of the ground-truth x_{gt} from a noisy observation y^δ of y , that is

$$(1.1) \quad y^\delta := y + \eta, \quad \|y^\delta - y\| \leq \delta,$$

where η is a random perturbation, typically unavoidable in practical scenarios, and $\delta > 0$ is the noise intensity.

The ill-posedness of K and the presence of noise force the introduction of a regularization strategy to solve our model equation. A standard variational method for (ME) reads

$$(1.2) \quad x_\alpha^\delta \in \operatorname{argmin}_{x \in X} \left\{ \frac{1}{2} \|Kx - y^\delta\|_2^2 + \alpha \|Lx\|_1 \right\},$$

*School of Mathematics (Zhuhai), Sun Yat-sen University, Zhuhai, 519082, China (bianchid@mail.sysu.edu.cn).

†Department of Computer Science and Engineering, University of Bologna, Bologna, 40126, Italy (dave.evangelista5@unibo.it, elena.loli@unibo.it).

‡Department of Science and High Technology, University of Insubria, Como, 22100, Italy (saleotti@uninsubria.it, marco.donatelli@uninsubria.it).

§School of Science, Harbin Institute of Technology, Shenzhen, Shenzhen, 518055, China (liwenbin@hit.edu.cn).

Funding: Davide Bianchi is supported by NSFC (Grant No. 12250410253). Marco Donatelli is partially supported by MIUR - PRIN 2022 N.2022ANC8HL and GNCS-INDAM. Wenbin Li is supported by Natural Science Foundation of Shenzhen (Grant No. JCYJ20190806144005645) and NSFC (Grant No. 41804096).

where L is a linear mapping, characterized by the property that $\ker(L) \cap \ker(K) = \{\mathbf{0}\}$, see [21, Chapter 8] and [43]. In this context, the term $\frac{1}{2}\|K\mathbf{x} - \mathbf{y}^\delta\|_2^2$ quantifies the fidelity of the reconstruction, the $\|L\mathbf{x}\|_1$ component serves as regularization term, and $\alpha > 0$ balances the trade-off between data fidelity and the regularization effect. Formulation (1.2) is a special case of generalized Tikhonov.

Typical choices for L include linear differential operators, especially for denoising applications involving signals that are nearly piecewise-constant, such as those encountered in imaging [29].

In the majority of the cases, L is a discretization of Euclidean first or second order linear differential operators, but the last decade has been seen an increasing interest for models and techniques from graph theory. In [25, 26], the authors introduced for the first time graph-based non-local operators for image segmentation and denoising problems; in [7, 10, 14, 39, 51] this approach is further investigated in the context of image deblurring and computerized tomography problems, and in [4, 45] it is applied to other different image processing inverse problems.

In essence, embedding a graph-based operator L in the regularization term acts as a guiding mechanism for the overall regularization process. This operator helps in identifying the “correct” neighborhood to concentrate the reconstruction efforts on, by capturing specific features that can be inferred from the observed signal \mathbf{y}^δ .

Initially, a graph structure G is constructed from a discretized signal to incorporate features such as interfaces and discontinuities. This discrete space, which heavily depends on the signal itself, can provide more insights into the neighborhood where \mathbf{x}_{gt} resides than a flat manifold like the Euclidean space.

Then, by choosing a suitable graph operator L , the optimization process in Equation (1.2) is oriented towards the (supposed) neighborhood of \mathbf{x}_{gt} .

The key point is to construct the graph from a signal that closely approximates the primary features of \mathbf{x}_{gt} . In [39], it was observed that generating the graph G directly from the observed and noisy data \mathbf{y}^δ results in poor outcomes for imaging tasks such as deblurring or tomographic reconstruction. This is because \mathbf{y}^δ exists in a different domain compared to \mathbf{x}_{gt} . To address this, the authors suggested an initial preprocessing step, transforming \mathbf{y}^δ to $\Psi(\mathbf{y}^\delta)$, and subsequently constructing a graph from $\Psi(\mathbf{y}^\delta)$. This preprocessing step involves a reconstruction map $\Psi: Y \rightarrow X$, from the space of observations Y to the domain X where \mathbf{x}_{gt} lives. This can be achieved, for example, by employing a standard Tikhonov filter [21] or the Filter Back Projection (FBP) method [34], depending on the inverse problem to handle. In the same spirit and independently, iterative schemes incorporating updates to graph weights were introduced in [4, 45, 51].

Taking inspiration from [39], we introduce the novel method **graphLa+ Ψ** . The initial preprocessing step involves selecting a family of reconstructor maps

$$\Psi_\Theta: Y \rightarrow X,$$

where $\Theta = \Theta(\delta, \mathbf{y}^\delta)$ is a family of parameters that can depend on δ and \mathbf{y}^δ . It is important to note that the pair (Ψ_Θ, Θ) is very general and may not be a convergent regularizing method.

Then, a graph G is built from $\Psi_\Theta^\delta := \Psi_\Theta(\mathbf{y}^\delta) \in X$, as well as its associated graph Laplacian operator $\Delta_{\Psi_\Theta^\delta}$ (see Section 2.1 for a proper definition). Finally, we find a minimizer of (1.2) with $L = \Delta_{\Psi_\Theta^\delta}$, that is,

$$(1.3) \quad \mathbf{x}_{\Psi_\Theta^\delta, \alpha}^\delta \in \underset{\mathbf{x} \in X}{\operatorname{argmin}} \left\{ \frac{1}{2} \|K\mathbf{x} - \mathbf{y}^\delta\|_2^2 + \alpha \|\Delta_{\Psi_\Theta^\delta} \mathbf{x}\|_1 \right\}.$$

Let us remark that the regularization term in (1.3) intrinsically relies on both the noise intensity δ and the observed data y^δ . This dependency introduces a layer of complexity into the analysis, making it highly non-standard.

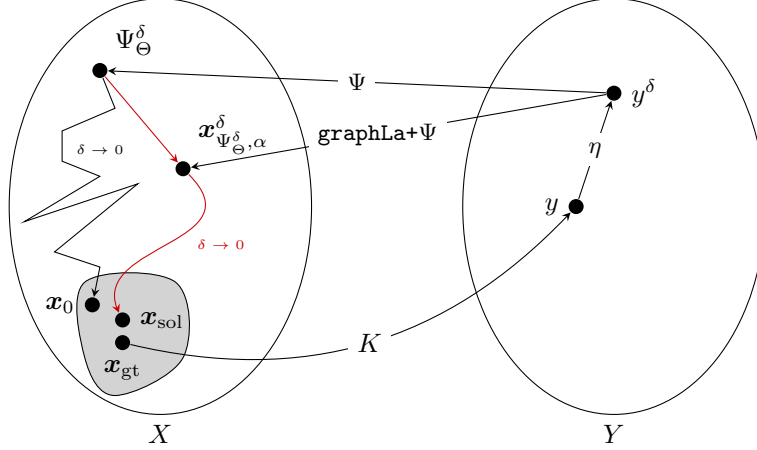


FIG. 1.1. A schematic representation of the **graphLa+ Ψ** method. The reconstructors Ψ_Θ do not necessarily need to be a regularization method, and this is represented by the piecewise linear path of Ψ_Θ^δ as $\delta \rightarrow 0$. However, when combined with the graph Laplacian in the Tikhonov method (1.2), it generates a convergent and stable regularization operator, that is, **graphLa+ Ψ** , which is represented by the smooth red path. See Sections 2 and 3 for more details on the notation.

In this study, we demonstrate that under certain, albeit very weak, hypotheses, **graphLa+ Ψ** is a convergent and stable regularization method in the limit as $\delta \rightarrow 0$. At the best of our knowledge, this is the first time that such a theoretical analysis has been carried out.

Properties of the graph Laplacian are the key ingredients. Informally speaking, it helps to “chain” the reconstructors Ψ_Θ in the original and well-established regularization method (1.2). See Figure 1.1 for a visual representation of the method.

For these reasons, and due to the minimal assumptions about Ψ_Θ , it becomes feasible to select reconstructors that may not be convergent regularizing methods, or those whose regularization properties lack rigorous proof yet show empirical effectiveness in certain applications. Owing to the influence of the graph Laplacian, the overall **graphLa+ Ψ** method maintains regularization and stability regardless.

In this context, a very interesting choice for Ψ_Θ is represented by the class of Deep Neural Networks (DNNs). They are highly nonlinear operators usually characterized by a paramount number of trainable parameters. Generally speaking, the set of parameters is trained by feeding the DNNs with a large number of data and minimizing a loss function. Thanks to the exponential increase of dedicated computational power, DNNs achieved state-of-the-art performances in various applications. Particularly in recent years, they have been extensively studied in the field of inverse problems, see [5] and references therein.

However, applying DNNs to ill-posed inverse problems presents notable drawbacks, most importantly instability and their “black-box” nature. Firstly, DNNs are often sensitive to data perturbations and have a tendency to produce hallucinations, i.e. false yet realistic-looking artifacts, see [3, 20]. Secondly, the complexity of their internal mechanisms, which involve millions of parameters and nonlinear mappings, makes them challenging to understand or explain [49].

These shortcomings contribute to a general mistrust in DNNs, particularly in real-world situations where accuracy, stability, and reliability are paramount, such as in medical applications. To address these concerns, we propose the integration of the **graphLa+ Ψ** method with a DNN, named **graphLa+Net**. This combination leverages the regularization properties of **graphLa+ Ψ** , resulting in a stable, convergent, and mathematically robust regularization method that incorporates a DNN, effectively countering the aforementioned flaws. An initial demonstration of the potential of **graphLa+Net** is presented in [11].

Our strategy with **graphLa+Net** follows other studies seeking to embed DNNs within a rigorous mathematical framework, see [12, 38, 44, 48]. This approach is crucial for the reliable application of DNNs to ill-posed inverse problems.

While the methodology and theory we develop herein apply broadly and are not limited solely to ill-posed inverse problems in imaging, to keep the paper self-contained we will focus on 2D computerized tomography (CT) applications.

The manuscript is organized as follows. [Section 2](#) introduces the notation and provides preliminaries on graph and regularization theories relevant to our model setting. This section particularly focuses on a general approach to generating a graph from an image. [Section 3](#) presents the **graphLa+ Ψ** method, covering its theoretical basis. In [Section 4](#), we specialize in the integration of the **graphLa+ Ψ** method with a DNN, namely **graphLa+Net**. [Sections 5](#) and [6](#) showcase numerical experiments within the CT framework, employing both synthetic and real data. These experiments demonstrate that the **graphLa+ Ψ** approach notably improves the quality of approximated solutions for each method Ψ , with **graphLa+Net** exhibiting exceptional performance, ensuring a robust and stable implementation of DNNs for solving inverse problems. In particular, thanks to the regularization property granted by the **graphLa+ Ψ** approach, we were able to avoid any estimate of the noise distribution during the DNN training, focusing only on the best accuracy performance of the DNN on an unperturbed dataset.

The manuscript concludes in [Section 7](#), where we summarize our findings and suggest future research directions. To maintain the readability and flow of the manuscript, the technical proofs involved in [Section 3](#) are moved in [Appendix A](#).

2. The model setting. Hereafter, we indicate in bold any finite dimensional (column) vector, i.e. $\mathbf{x} \in X \simeq \mathbb{R}^n$, and for the p -component of \mathbf{x} we write $\mathbf{x}(p)$, for $p = 1, \dots, n$. We use the standard notation $\|\cdot\|_r$ for an ℓ^r -norm, $r \in [1, \infty]$.

As a baseline assumption we say that the unperturbed observation $\mathbf{y} \in Y \simeq \mathbb{R}^m$, which is given in (1.1) for $\delta = 0$, is the realization of the action of K on an element $\mathbf{x}_{\text{gt}} \in X$. That is,

Hypothesis 2.1. There exists \mathbf{x}_{gt} such that $K\mathbf{x}_{\text{gt}} = \mathbf{y}$.

On the one hand, the goal is to obtain a reliable approximation of the ground truth signal \mathbf{x}_{gt} when we have access only to an observation \mathbf{y}^δ corrupted by unknown noise. On the other hand, the unperturbed system (ME) for $\delta = 0$ can be underdetermined, the observed data \mathbf{y}^δ can not belong to the range of K , or the (pseudo) inverse of K can be very sensitive even to small levels of $\delta > 0$. For those reasons, we say that the inverse problem of finding a solution for (ME) is ill-posed, and need to be regularized. For an overview of ill-posed inverse problems and regularization techniques, we refer the reader to [21, 28, 47].

Our analysis will heavily depend on graph structures, and so in [Subsection 2.1](#) we provide the groundwork of Graph Theory, and in [Subsection 2.2](#) we explore the

relationship between images and graphs. This relationship will be exploited in the numerical experiments of [Section 6](#).

2.1. Graph Theory. Fix a finite set P . We indicate by $C(P)$ the set of real-valued functions on P , that is,

$$C(P) := \{\mathbf{x} \mid \mathbf{x} : P \rightarrow \mathbb{R}\}.$$

Assuming an implicit ordering of the elements in P , it is evident that if the cardinality of the set P is n then $C(P) \simeq \mathbb{R}^n \simeq X$. Hence, we use the same notation for finite-dimensional vectors, even when referring to elements $\mathbf{x} \in C(P)$. From [Section 3](#) we will often make the identifications $C(P) = \mathbb{R}^n = X$.

For a detailed introduction to the graph setting as presented here, see [\[35\]](#).

DEFINITION 2.2. A graph over a finite set P is a pair $G = (w, \mu)$ given by:

- A nonnegative edge-weight function $w : P \times P \rightarrow [0, \infty)$ that satisfies
 - i) Symmetry: $w(p, q) = w(q, p)$ for every $p, q \in P$;
 - ii) No loops: $w(p, p) = 0$ for every $p \in P$.
- A positive node measure $\mu : P \rightarrow (0, \infty)$.

Two nodes are connected if $w(p, q) > 0$, and in that case we write $p \sim q$. A finite walk is a finite sequence of nodes $\{p_i\}_{i=0}^k$ such that $w(p_i, p_{i+1}) > 0$ for $i = 0, \dots, k-1$. A subset $Q \subseteq P$ is *connected* if for every pair of nodes $p, q \in Q$ there is a finite walk such that $p_0 = p$, $p_k = q$, and each p_i belongs to Q . A connected subset $Q \subseteq P$ is a *connected component* of P if it is maximal with respect to the ordering of inclusion.

DEFINITION 2.3 (graph Laplacian). The graph Laplacian $\Delta : C(P) \rightarrow C(P)$ associated to the graph $G = (w, \mu)$ is defined by the action

$$\Delta \mathbf{x}(p) := \frac{1}{\mu(p)} \sum_{q \in P} w(p, q) (\mathbf{x}(p) - \mathbf{x}(q)).$$

Notice that Δ does not depend on the ordering (or labeling) of the elements in P .

2.1.1. Construction of a graph from an element of $C(P)$. Given a finite set $P = \{p \mid p = 1, \dots, n\}$, fix a distance $\text{dist}(\cdot, \cdot)$ on the set P and a nonnegative function $h_d : \mathbb{R} \rightarrow [0, +\infty)$ such that $h_d(0) = 0$. Then it follows easily that

$$w_d(p, q) := h_d(\text{dist}(p, q))$$

is an edge-weight function on P , since w_d satisfies [Items i\)](#) and [ii\)](#) from [Definition 2.2](#). It is based on the geometric properties of P induced by the distance $\text{dist}(\cdot, \cdot)$. The magnitude of the connections between two nodes p and q is then regulated by h_d .

Fix now an element $\mathbf{x} \in C(P)$, another nonnegative function $h_i : \mathbb{R} \rightarrow [0, +\infty)$ and finally define

$$(2.1) \quad w_{\mathbf{x}}(p, q) := \underbrace{w_d(p, q)}_{\text{geometry}} \cdot \underbrace{h_i(|\mathbf{x}(p) - \mathbf{x}(q)|)}_{\mathbf{x} \text{ intensity}}.$$

The edge-weight function [\(2.1\)](#) between two nodes depends on both the “physical” distance, thanks to w_d , and the “variation of intensity” of \mathbf{x} , thanks to $h_i(|\mathbf{x}(p) - \mathbf{x}(q)|)$. This dual dependence has a twofold effect: it can separate nodes that reside in different and unrelated regions of the space, and it weights the magnitude of the connections

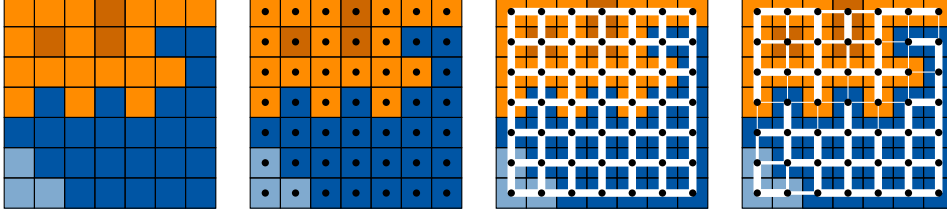


FIG. 2.1. Simple outline of how to build a graph from an image \mathbf{x} . To be read from left to right. Left: a 7×7 pixels image made by orange-like and blue-like square pixels. The color intensity of each pixel is given by the pixel-wise evaluation of a function \mathbf{x} . Center-left: each pixel corresponds one node, represented by a black circle. Since the pixels are disposed on a grid, each node can be associated to an ordered pair in \mathbb{Z}^2 . Center-right: the geometric edge-weight function w_d in (2.1) is given by $\mathbb{1}_{(0,1]}(\|p - q\|_\infty)$, that is, two nodes p, q are connected if and only if $\|p - q\|_\infty = 1$, and in that case the magnitude of the connection is one. Right: the magnitude of an edge between two nodes is then weighted by $h_i(\|\mathbf{x}(p) - \mathbf{x}(q)\|) \in (0, 1]$, where h_i is the Gaussian function, see (2.3). The role of h_i is to measure the difference of intensity between two adjacent pixels, and it is close to zero when two pixels have very different color intensities. This is represented by the different thickness of the edges connecting two adjacent pixels, where a thick edge means very similar color intensity and a thin edge means a very different color intensity.

depending on the difference of intensities of \mathbf{x} . For an example of application, see Subsection 2.2.

Now choose any strictly positive function, which may depend on \mathbf{x} ,

$$(2.2) \quad \mu_{\mathbf{x}}(p) > 0 \quad \forall p \in P.$$

Therefore, following Definition 2.2, for any fixed $\mathbf{x} \in C(P)$, the pair (2.1)-(2.2) is a graph G , on the set P , induced by \mathbf{x} . We will write then $\Delta_{\mathbf{x}}$ to indicate the associated graph Laplacian, as per Definition 2.3.

2.2. Images and graphs. We briefly describe here how images and graphs can be related, following the strategy and notation described in the previous Subsection 2.1.1, and provide a practical example.

First, any image is made by the union of several pixels $p \in P$ disposed on a grid of dimension $d_1 \times d_2$, where $d_1, d_2 \in \mathbb{N}$. It is then natural to identify them as ordered pairs $p = (i, j) \in \mathbb{Z}^2$ with $i = 1, \dots, d_1$ and $j = 1, \dots, d_2$.

As a consequence, a reasonable choice to connect two pixels by their “physical” distance is to set

$$\text{dist}(p, q) := \|p - q\|_\infty \quad \text{and} \quad h_d(t) := \mathbb{1}_{(0, R]}(t),$$

where $\mathbb{1}_{(0, R]}$ is the indicator function of the set $(0, R]$ and R is a parameter of control which tells the maximum distance allowed for two pixels to be neighbors. If $0 < \|p - q\|_\infty \leq R$, then p and q are connected with an edge of magnitude 1, viz. $w_d(p, q) = 1$.

Second, a gray-scale image is given by the light intensities of its pixels. That is, a gray-scale image can be represented by a function $\mathbf{x} \in C(P)$ such that $\mathbf{x}(p) \in [0, 1]$, where 0 means black and 1 means white. A common choice to weight the connection of two different pixels by their light intensities is to use the Gaussian function, that is

$$h_i(t) := e^{-\frac{t^2}{\sigma^2}}, \quad \sigma > 0.$$

The reason lies on the relationship between the heat kernel and the discretization of the Laplacian on a manifold. See [13] for discussions about the Laplacian on

discretized manifolds, and [17] for another application of the Gaussian function to define the weights of the graph Laplacian.

We arrive then at the definition of the edge-weight function in (2.1), applied to our case, that is

$$(2.3) \quad w_{\mathbf{x}}(p, q) = \mathbb{1}_{(0, R]}(\|p - q\|_{\infty}) e^{-\frac{|\mathbf{x}(p) - \mathbf{x}(q)|^2}{\sigma^2}}.$$

For colored images, it is a little bit different. For example, in the RGB representation, the color of a pixel is given by the combination of the light intensities of three channels R(ed), G(reen) and B(lue). Therefore, in principle a colored image should be regarded as a function $\mathbf{x} : P \rightarrow \mathbb{R}^3$, where $\mathbf{x}(p) = (\mathbf{x}_R(p), \mathbf{x}_G(p), \mathbf{x}_B(p))$ is a vector-valued function whose elements represent the light intensities for each channel. However, it is common to assume that the ill-posed operator K acts independently on each channel, and therefore the regularization is made on each channel separately. If for some reasons this assumption can not be made, then we can simply modify the definition of (2.1) in the following way:

$$w_{\mathbf{x}}(p, q) := w_d(p, q) \cdot h_i(\|\mathbf{x}(p) - \mathbf{x}(q)\|),$$

where $\|\cdot\|$ is any appropriate norm in \mathbb{R}^3 . See Figure 2.1 for a simple example of building a graph from an image.

3. The graphLa+Ψ regularization method. In this section we introduce the graphLa+Ψ method and we show that it is a regularization method.

Let us begin by considering a family of operators $\{\Psi_{\Theta} : Y \rightarrow X\}$ which we generally refer to as *reconstructors*. Ψ_{Θ} is not necessarily linear, and $\Theta \in \mathbb{R}^k$ denotes its parameters. This family of reconstructors is at the core of our graphLa+Ψ method. It has the very important role to give a first approximation of \mathbf{x}_{gt} , since upon this approximation the reconstruction step of our method is built.

We need to enforce some (weak) regularity on Ψ_{Θ} . Assume that there exists an element $\mathbf{x}_0 \in X$, a nonnegative function $g = g(\delta, \mathbf{x}_0)$, and a parameter choice rule $\Theta = \Theta(\delta, \mathbf{y}^{\delta})$ such that

Hypothesis 3.1.

$$\|\Psi_{\Theta(\delta, \mathbf{y}^{\delta})}(\mathbf{y}^{\delta}) - \mathbf{x}_0\|_2 \leq g(\delta, \mathbf{x}_0) \rightarrow 0 \quad \text{as } \delta \rightarrow 0.$$

The above Hypothesis 3.1 will guarantee that the graphLa+Ψ method, which we will introduce properly in (3.1), is a convergent regularization method. Let now \mathbf{y}^{δ} and $\Theta := \Theta(\delta, \mathbf{y}^{\delta})$ be fixed, and $\{\delta_k\}$ and $\{\mathbf{y}^{\delta_k}\}$ be sequences such that $\delta_k \rightarrow \delta$ and $\mathbf{y}^{\delta_k} \rightarrow \mathbf{y}^{\delta}$ for $k \rightarrow \infty$. Write $\Theta_k := \Theta(\delta_k, \mathbf{y}^{\delta_k})$. The next hypothesis will guarantee stability for (3.1).

Hypothesis 3.2.

$$\Theta_k \rightarrow \Theta \quad \text{and} \quad \|\Psi_{\Theta_k}(\mathbf{y}^{\delta_k}) - \Psi_{\Theta}(\mathbf{y}^{\delta})\|_2 \leq f(k) \rightarrow 0 \text{ for } k \rightarrow \infty.$$

In the next two examples, we make clear that the above assumptions are pretty weak and they can be satisfied by several large classes of reconstructors. In particular, the pair (Ψ_{Θ}, Θ) does not need to be a convergent regularization method.

EXAMPLE 3.3. A simple example of a family of reconstructors that satisfies Hypothesis 3.1 is the case when we identify them with a single, (locally) Lipschitz continuous operator. That is, fix $\Theta \equiv \hat{\Theta}$ for every δ and \mathbf{y}^{δ} , and choose an operator

$\Psi_{\hat{\Theta}}$ such that $\|\Psi_{\hat{\Theta}}(\mathbf{y}_1) - \Psi_{\hat{\Theta}}(\mathbf{y}_2)\|_2 \leq c\|\mathbf{y}_1 - \mathbf{y}_2\|_2$. Thanks to (1.1) and the Lipschitz condition, [Hypothesis 3.1](#) is then trivially verified with $\mathbf{x}_0 := \Psi_{\hat{\Theta}}(\mathbf{y})$ and $g(\delta, \mathbf{x}_0) = c\delta$. In the same way, [Hypothesis 3.2](#) is verified by $f(k) = c\|\mathbf{y}^{\delta_k} - \mathbf{y}^\delta\|$.

The situation of the preceding example will occur later, when $\Psi_{\hat{\Theta}}$ is implemented as a trained DNN, as discussed in [Section 4](#) and [subsection 5.3](#). Let us emphasize that DNNs are typically non-regularizing methods.

EXAMPLE 3.4. A less trivial family of reconstructors that satisfy [Hypothesis 3.1](#) is the one given by any typical regularization operators, as per [21, Definition 3.1], for example. Let $\Theta \in (0, \infty)$ and Ψ_Θ be continuous, and K^\dagger be the usual Moore-Penrose pseudo-inverse of K . Fix $\mathbf{x}_0 := K^\dagger \mathbf{y}$ and observe that $K\mathbf{x}_0 = \mathbf{y}$, since $\mathbf{y} \in \text{range}(K)$ by [Hypothesis 2.1](#). By definition of regularization operator, there exists a parameter choice rule $\Theta = \Theta(\delta, \mathbf{y}^\delta)$ such that

$$g(\delta, \mathbf{x}_0) := \sup\{\|\Psi_{\Theta(\delta, \mathbf{y}^\delta)}(\mathbf{y}^\delta) - \mathbf{x}_0\|_2 \mid \mathbf{y}^\delta \in Y, \|\mathbf{y}^\delta - K\mathbf{x}_0\|_2 \leq \delta\} \rightarrow 0 \quad \text{as } \delta \rightarrow 0,$$

and [Hypothesis 3.1](#) is then verified. About [Hypothesis 3.2](#), this is a bit more involved and depends on the regularization method itself and the parameter choice rule. We will show a specific example in [Appendix A](#).

The class of convergent regularization methods which fits [Example 3.4](#) is vast, and not necessarily restricted to the Hilbert setting. We mention Tikhonov-Phillips methods (both ordinary and iterative variants) [8, 9, 31, 36], popular ℓ^p - ℓ^q methods with general regularization term [19, 37], and framelets [15, 16, 32].

As detailed in [Subsection 2.1.1](#), we can define a graph Laplacian induced by

$$\Psi_\Theta^\delta := \Psi_\Theta(\mathbf{y}^\delta) \in X \simeq C(P),$$

and we will denote it by $\Delta_{\Psi_\Theta^\delta}$. Consider then the following Tikhonov-type variational method for [\(ME\)](#),

$$(3.1) \quad \mathbf{x}_{\Psi_\Theta^\delta, \alpha}^\delta \in \operatorname{argmin}_{\mathbf{x} \in X} \left\{ \frac{1}{2} \|K\mathbf{x} - \mathbf{y}^\delta\|_2^2 + \alpha \|\Delta_{\Psi_\Theta^\delta} \mathbf{x}\|_1 \right\}.$$

We call [\(3.1\)](#) the **graphLa+ Ψ** method.

Let us focus our attention on the regularization term $\mathcal{R}(\mathbf{x}, \mathbf{y}^\delta) := \|\Delta_{\Psi_\Theta^\delta} \mathbf{x}\|_1$. As a first remark, notice that, unlike typical regularization methods, \mathcal{R} depends not only on \mathbf{x} but also on the data \mathbf{y}^δ . This complicates any attempt at studying the convergence of [\(3.1\)](#) for $\delta \rightarrow 0$.

As a second remark, indicating with $w_{\Psi_\Theta^\delta}$ the edge-weight function [\(2.1\)](#) with \mathbf{x} replaced by Ψ_Θ^δ , we have that minimizing \mathcal{R} means to force $\mathbf{x}_{\Psi_\Theta^\delta, \alpha}^\delta$ to be constant on the regions where $w_{\Psi_\Theta^\delta}(p, q)$ is “large”. This is a direct consequence of [Definition 2.3](#),

$$|\Delta_{\Psi_\Theta^\delta} \mathbf{x}(p)| = \frac{1}{\mu_{\Psi_\Theta^\delta}(p)} \left| \sum_{q \in P} w_{\Psi_\Theta^\delta}(p, q)(\mathbf{x}(p) - \mathbf{x}(q)) \right|.$$

For example, setting $w_{\Psi_\Theta^\delta}$ as in [\(2.3\)](#), then $w_{\Psi_\Theta^\delta}(p, q)$ attains its maximum value of 1 if and only if $p \sim q$ and $\Psi_\Theta^\delta(p) = \Psi_\Theta^\delta(q)$. Therefore, $\|\Delta_{\Psi_\Theta^\delta} \mathbf{x}\|_1 \approx 0$ if \mathbf{x} is constant on the regions where Ψ_Θ^δ is constant.

Put simply, we can say that \mathcal{R} helps to distinguish the regions of uniformity from the regions of interfaces. In intuition, once Ψ_Θ^δ reconstructs the region of interfaces in

\mathbf{x}_{gt} , the final solution $\mathbf{x}_{\Psi_{\Theta}^{\delta}, \alpha}$ will be a good approximation of the ground truth \mathbf{x}_{gt} , even though Ψ_{Θ}^{δ} deviates from \mathbf{x}_{gt} in other aspects.

As a last comment, the ℓ^1 -norm in \mathcal{R} is introduced to enforce sparsity on the approximated solution $\mathbf{x}_{\Psi_{\Theta}^{\delta}, \alpha}$. This is mainly in view of the imaging applications of Section 6. All the theory developed here works with the ℓ^1 -norm replaced by any ℓ^r -norm for $r > 1$.

3.1. Convergence and stability results. In this subsection we study the regularizing properties of **graphLa+Ψ**. Since the proofs involved are quite technical, to help the readability of this subsection we move them to [Appendix A](#).

First, we need a definition of solution for (ME). Under [Hypothesis 3.1](#), let \mathbf{x}_0 and $\Theta = \Theta(\delta, \mathbf{y}^{\delta})$ be such that

$$(3.2) \quad \mathbf{x}_0 := \lim_{\delta \rightarrow 0} \Psi_{\Theta(\delta, \mathbf{y}^{\delta})}(\mathbf{y}^{\delta}).$$

DEFINITION 3.5. We call \mathbf{x}_{sol} a graph-minimizing solution with respect to \mathbf{x}_0 , defined in (3.2), if $K\mathbf{x}_{\text{sol}} = \mathbf{y}$ and

$$(3.3) \quad \|\Delta_{\mathbf{x}_0} \mathbf{x}_{\text{sol}}\|_1 = \min\{\|\Delta_{\mathbf{x}_0} \mathbf{x}\|_1 \mid \mathbf{x} \in X, K\mathbf{x} = \mathbf{y}\}.$$

Let us indicate with $w_{\Psi_{\Theta}^{\delta}}$ and w_0 the edge-weight functions in (2.1) induced by Ψ_{Θ}^{δ} and \mathbf{x}_0 , respectively. To make our analysis work, we need three last hypotheses which are related to properties of $w_{\Psi_{\Theta}^{\delta}}$ and $\Delta_{\Psi_{\Theta}^{\delta}}$. As we will discuss here, those hypotheses are easy to be satisfied.

Hypothesis 3.6. For every $p, q \in P$, $w_{\Psi_{\Theta}^{\delta}} > 0$ if and only if $w_0(p, q) > 0$.

The following lemma is an immediate consequence of the above hypothesis.

LEMMA 3.7. Under [Hypothesis 3.6](#), there is an invariant subspace $V \subseteq C(P)$ such that $\ker(\Delta_{\Psi_{\Theta}^{\delta}}) = \ker(\Delta_{\mathbf{x}_0}) = V$ for every Ψ_{Θ}^{δ} .

Proof. See [Appendix A](#). □

The invariant subspace V replaces $\ker(L)$ in the typical null-space condition $\ker(K) \cap \ker(L) = \{\mathbf{0}\}$, invoked for functionals of the form (1.2).

Hypothesis 3.8. $\ker(K) \cap V = \{\mathbf{0}\}$.

The above hypotheses are not difficult to check in practice. Indeed, the null space of the graph Laplacian is given by the constant functions on the connected components of P . So, for example, from (2.1), if P is connected with respect to w_d and h_i is strictly positive, then P is connected with respect to the edge-weight function $w_{\mathbf{x}}$ for any $\mathbf{x} \in C(P)$. As a consequence, $\ker(\Delta_{\Psi_{\Theta}^{\delta}}) = \{t\mathbf{1} \mid t \in \mathbb{R}\}$ for any $\Psi_{\Theta}^{\delta} \in C(P)$, where we indicate with $\mathbf{1}$ the vector whose elements are all ones.

The last assumption we need is on the function h_i in (2.1) and the node measure $\mu_{\mathbf{x}}$ in (2.2).

Hypothesis 3.9. The function h_i and the map $\mathbf{x} \mapsto \mu_{\mathbf{x}}(p)$, for every fixed $p \in P$, are locally Lipschitz.

In [Section 6](#), we will provide specific choices of (2.1) and (2.2) for our numerical experiments, where we will show that [Hypotheses 3.6, 3.8, and 3.9](#) are satisfied.

Throughout the remainder of this section, we will assume the validity of all the hypotheses introduced thus far: [Hypotheses 2.1, 3.1, 3.6, 3.8, and 3.9](#).

The first three results are about existence and uniqueness of the graph-minimizing solution and the well-posedness of (3.1).

PROPOSITION 3.10. *There exists a graph-minimizing solution \mathbf{x}_{sol} .*

Proof. See Appendix A. \square

PROPOSITION 3.11. *For every fixed $\delta, \alpha > 0$ and $\mathbf{y}^\delta \in Y$, there exists a solution $\mathbf{x}_{\Psi_\Theta^\delta, \alpha}^\delta$ for the variational problem (3.1).*

Proof. See Appendix A. \square

COROLLARY 3.12. *If K is injective, then \mathbf{x}_{sol} and $\mathbf{x}_{\Psi_\Theta^\delta, \alpha}^\delta$ are unique.*

Proof. See Appendix A. \square

Remark 3.13. Without the injectivity property, uniqueness can fail. The main culprit is the ℓ^1 -norm in the regularization term. However, it is possible to achieve uniqueness in a less stringent manner, namely, for every \mathbf{y}^δ outside a set of negligible measure. The approach should be in line with [2, 18], but adapted to this specific context. That being said, relaxing the assumptions to regain uniqueness of the solutions falls beyond the scope of the current work.

The next theorems provide convergence and stability results.

THEOREM 3.14. *Assume that $\alpha: (0, +\infty) \rightarrow (0, +\infty)$ satisfies*

$$(3.4a) \quad \lim_{\delta \rightarrow 0} \alpha(\delta) = 0,$$

$$(3.4b) \quad \lim_{\delta \rightarrow 0} \frac{\delta^2}{\alpha(\delta)} = 0.$$

Fix a sequence $\{\delta_k\}$ such that

$$\lim_{k \rightarrow \infty} \delta_k = 0, \quad \|\mathbf{y}^{\delta_k} - \mathbf{y}\|_2 \leq \delta_k,$$

and set $\alpha_k := \alpha(\delta_k)$. Let $\Theta = \Theta(\delta, \mathbf{y}^\delta)$ be the parameter choice rule as in Hypothesis 3.1, and set $\Theta_k := \Theta(\delta_k, \mathbf{y}^{\delta_k})$. Then every sequence $\{\mathbf{x}_k\}$ of elements that minimize the functional (3.1), with δ_k and Θ_k , has a convergent subsequence. The limit \mathbf{x}_{sol} of the convergent subsequence $\{\mathbf{x}_{k'}\}$ is a graph-minimizing solution with respect to \mathbf{x}_0 , and

$$\lim_{k'} \|\Delta_{\Psi_{\Theta_{k'}}^{\delta_{k'}}} \mathbf{x}_{k'}\|_1 = \|\Delta_{\mathbf{x}_0} \mathbf{x}_{\text{sol}}\|_1.$$

If \mathbf{x}_{sol} is unique, then $\mathbf{x}_k \rightarrow \mathbf{x}_{\text{sol}}$.

Proof. See Appendix A. \square

THEOREM 3.15. *Let now \mathbf{y}^δ be fixed and $\{\delta_k\}$ and $\{\mathbf{y}^{\delta_k}\}$ be sequences such that $\delta_k \rightarrow \delta$ and $\mathbf{y}^{\delta_k} \rightarrow \mathbf{y}^\delta$ for $k \rightarrow \infty$. Then every sequence $\{\mathbf{x}_k\}$ with*

$$\mathbf{x}_k \in \operatorname{argmin}_{\mathbf{x} \in X} \left\{ \frac{1}{2} \|K\mathbf{x} - \mathbf{y}^{\delta_k}\|_2^2 + \alpha \|\Delta_{\Psi_{\Theta_k}^{\delta_k}} \mathbf{x}\|_1 \right\},$$

has a converging subsequence $\{\mathbf{x}_{k'}\}$ such that

$$\lim_{k'} \mathbf{x}_{k'} \in \operatorname{argmin}_{\mathbf{x} \in X} \left\{ \frac{1}{2} \|K\mathbf{x} - \mathbf{y}^\delta\|_2^2 + \alpha \|\Delta_{\Psi_\Theta^\delta} \mathbf{x}\|_1 \right\}.$$

Proof. See [Appendix A](#). \square

4. graphLa+Net. Among the possible choices for reconstructors Ψ_{Θ} , we propose to use a Deep Neural Network (DNN). In this case, the set of parameters Θ contains matrices and vectors, which are the building blocks of DNNs. For a mathematical introduction to neural networks we refer to [30]. Informally speaking, a DNN is a long chain of compositions of affine operators and nonlinear activation functions. The set of parameters Θ is then trained by minimizing a loss function over a large number of data, see [Subsection 5.3](#). When considering Ψ_{Θ} as a DNN, we specify it by calling the method **graphLa+Net**. A first overview of **graphLa+Net** was proposed in [11].

Note that, in principle, it is possible to make the network parameters Θ dependent on the noise level δ by training it multiple times for different values of δ . However, this is rarely done in practice due to the significant amount of time and energy consumption it would require. This limitation has always been a crucial challenge in employing DNNs for regularizing ill-posed problems, as it necessitates the estimate of an optimal noise level δ which is suitable for diverse applications. Additionally, opting for $\delta = 0$ is generally not a good choice due to the typical high sensitivity of DNNs to the noise.

Nonetheless, the regularizing property of **graphLa+ Ψ** effectively addresses this issue. In the subsequent discussion, we will consider DNNs as reconstructors with a fixed $\hat{\Theta}$, where $\hat{\Theta}$ has been trained over a *noiseless* dataset. As will be shown in [Subsections 6.1](#) and [6.2](#), the resulting **graphLa+Net** is not only regularizing and stable but also significantly superior in performance, despite the inherent instability of the original DNN.

4.1. The architecture. In our DNN model, we utilize a modified version of the U-net, as detailed in [46]. The structure of this modified U-net is illustrated in [Figure 4.1](#). U-net is a widely recognized multi-scale Convolutional Neural Network architecture, known for its effectiveness in processing images with global artifacts. This fully convolutional network features a symmetrical encoder-decoder structure, employing strided convolutions to expand its receptive field. The encoder layers' strides create distinct levels of resolution within the network. Each level comprises a set number of blocks, where a block consists of a convolutional layer with a fixed number of channels, followed by batch normalization and a ReLU activation function. The number of convolutional channels is doubled at each successive level, starting from a baseline number in the first layer. Specifically, our network is designed with four levels and a baseline of 64 convolutional channels.

As mentioned, the decoder mirrors the encoder but uses upsampling convolutional layers in place of strided convolutions. Furthermore, to preserve high-frequency details, skip connections link the final layer of each encoder level to the corresponding first layer of the decoder.

The network we consider in this paper is called *Residual U-net (ResU-net)* and it was proposed in [23]. This network is a variation of the original U-net architecture, modified through two key changes. First, we have reconfigured the skip connections to work as additions rather than concatenations, a strategy aimed at reducing the total number of parameters. Second, we introduce a residual connection that links the input and output layers directly, which implies that the network learns the residual mapping between the input and the expected output. The importance of the residual connection has been observed in [27], where the authors proved that the residual manifold containing the artifacts is easier to learn than the true image manifold.

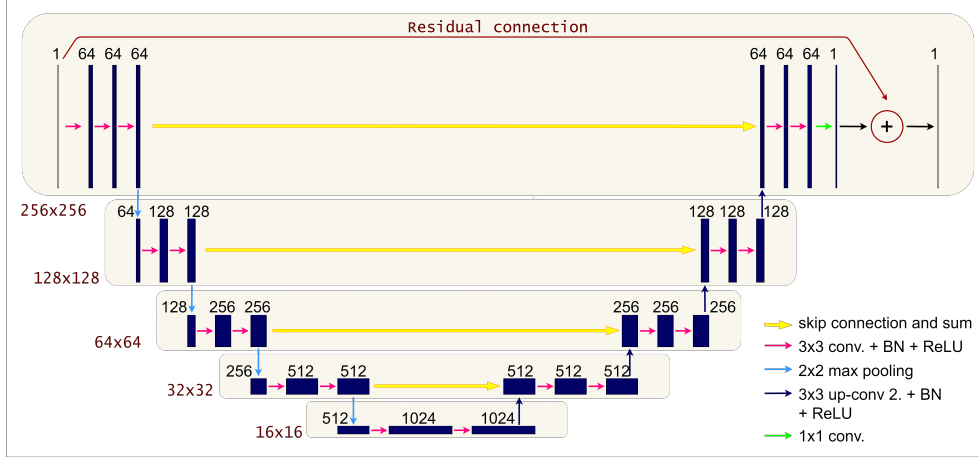


FIG. 4.1. A diagram of the ResU-net architecture used in the experiments.

5. Experimental setup. In this section we describe the setting of the **graphLa+ Ψ** method in our numerical experiment.

5.1. Sparse view Computed Tomography. X-rays Computed Tomography (CT) is a widespread imaging system particularly useful to detect injuries, tumors, internal bleeding, bone fractures, and various medical conditions. It is essentially constituted by a source rotating around an object and emitting X-rays beams from a fixed number of angles along its arc trajectory. Passing through the interior of the object, a quantity of radiation proportional to the density of the tissues gets absorbed and the resulting rays are measured by a detector. The collection of all the measurements at different projection angles is called the sinogram.

In this case, the matrix $K \in \mathbb{R}^{m \times n}$ represents the discrete Radon operator, $\mathbf{x} \in \mathbb{R}^n$ is the 2D object discretized in n pixels (voxels) and $\mathbf{y}^\delta \in \mathbb{R}^m$ is the sinogram. Here, the dimension m depends on the number of projection angles n_α . In medical applications, sparse view CT denotes the case where only a small number of angles n_α is considered, in order to reduce the radiation dose absorbed by the patient. In this particular setting, the matrix K is under-determined (i.e. $m < n$). To faithfully simulate the real medical scenario in our experiments we model K as the fan beam Radon transform, modeling the spread of X-rays with a fan trajectory.

5.2. The datasets and the test problem. We evaluate the **graphLa+ Ψ** algorithms using two distinct image datasets. The first is the COULE dataset, which comprises synthetic images with a resolution of 256x256 pixels. These images feature ellipses and lines of varying gray intensities against a dark background. This dataset is publicly available on Kaggle [22]. The second dataset is a subsampled version of the AAPM Low Dose CT Grand Challenge dataset, provided by the Mayo Clinic [40]. It contains real chest CT image acquisitions, each also at a resolution of 256x256 pixels.

To simulate the sinogram \mathbf{y}^δ we consider n_α different angles evenly distributed within the closed interval $[0, 179]$, where $n_\alpha = 120$ in the experiments with COULE dataset and $n_\alpha = 180$ in the experiments with Mayo dataset. The sinograms are generated using the IRtools toolbox [24].

In Figures 5.1 and 5.2, we present an example of the true image and its resulting

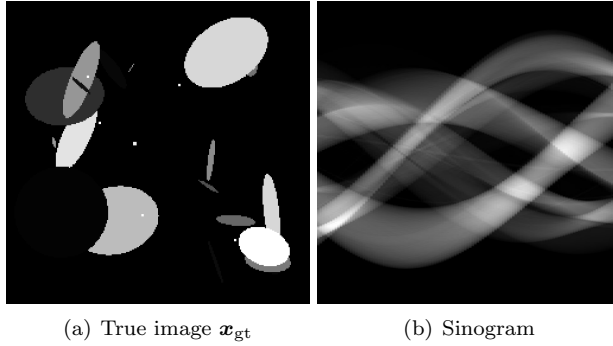


FIG. 5.1. (a): Example of a \mathbf{x}_{gt} image from COULE dataset. (b): The resulting sinogram

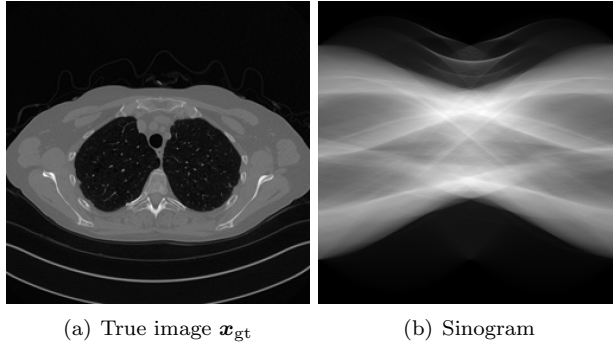


FIG. 5.2. (a): Example of a \mathbf{x}_{gt} image from Mayo dataset. (b): The resulting sinogram

sinogram of size $n_d \times n_\alpha$, where $n_d = \lfloor \sqrt{2n} \rfloor$ is the number of pixels of the detector. To simulate real-world conditions, we add white Gaussian noise $\boldsymbol{\xi}$ to the sinogram at an intensity level of δ , indicating that the norm of the noise is δ times the norm of the sinogram. In particular, we compute \mathbf{y}^δ as:

$$\mathbf{y}^\delta = \mathbf{y} + \delta \|\mathbf{y}\| \frac{\boldsymbol{\xi}}{\|\boldsymbol{\xi}\|}.$$

5.3. Neural Network training. We randomly select 400 pairs of images from COULE and 3,305 pairs of images from Mayo as training sets, all of the form $(\mathbf{x}_{\text{gt}}, \mathbf{y}^\delta)$. Following the discussion in Section 4, we train the DNN over the training sets in a supervised manner without extra noise, specifically by setting $\delta = 0$. The process involves finding $\hat{\Theta}$ that minimizes the Mean Squared Error between the predicted reconstruction $\Psi_\Theta(\mathbf{y})$ and the ground-truth solution \mathbf{x}_{gt} . Once the training process is completed, we set $\Theta \equiv \hat{\Theta}$.

Since the ResU-net architecture is fully convolutional, the input required by the network is an image. Hence, the input sinogram \mathbf{y} has to be pre-processed through a fast algorithm mapping the sinogram to a coarse reconstructed image, such as FBP [33, 41] or a few iterations of a regularizing algorithm [23, 42]. For those experiments, we choose the FBP.

The networks has been trained on an NVIDIA RTX A4000 GPU card with 16Gb

of VRAM, for a total of 50 epochs and a batch size of 10. We use Adam optimizer with a learning rate of 0.001, $\beta_1 = 0.9$, and $\beta_2 = 0.999$, in all the experiments.

6. Numerical experiments. In the numerical example, to compute the graph Laplacian we consider the edge-weight function $\omega_{\mathbf{x}}$ defined as in (2.3), and the node function $\mu_{\mathbf{x}}$ in the following form

$$(6.1) \quad \mu_{\mathbf{x}}(p) := \sqrt{\sum_{p,q \in P} w_{\mathbf{x}}^2(p, q)}.$$

It is straightforward to check that $h_i = e^{-\frac{t^2}{\sigma^2}}$ used in (2.3) is Lipschitz, and so $\mathbf{x} \mapsto \mu_{\mathbf{x}}(p)$ is locally Lipschitz for every $p \in P$. Therefore, the choices (2.3) and (6.1) satisfy Hypothesis 3.9.

To find approximate solution of our $\ell^2 - \ell^1$ model (3.1), we use a Majorization–Minimization strategy combined with a Generalized Krilov Subspace approach; we refer readers to [37] for the details of the algorithm.

This section is divided into two parts, with each part concentrating on tests for a specific dataset. In both scenarios, we rigorously examined the performance of the **graphLa+ Ψ** method to provide a comprehensive analysis of the method’s robustness and adaptability.

More in details, we consider a wide range of reconstructors Ψ , including Filter Back Projection (**graphLa+FBP**), standard Tikhonov (**graphLa+Tik**), Total Variation (**graphLa+TV**), and the trained DNN (**graphLa+Net**) described in the previous Section 4. In all cases, the ground truth images \mathbf{x}_{gt} are drawn outside of the training sets defined for the DNN in Subsection 5.3.

The regularization parameters that appear in the Tikhonov and TV methods are calculated using Generalized Cross Validation and the discrepancy principle, respectively.

For comparison, we will include the reconstruction achieved by our method using the ground truth image \mathbf{x}_{gt} as a first approximation, labeled as **graphLa+ \mathbf{x}_{gt}** . This serves as an upper bound reference for the effectiveness of all the **graphLa+ Ψ** methods.

The quantitative results of our experiments will be measured by the reconstruction relative error (RRE) and peak signal-to-noise ratio (PSNR), where

$$\text{RRE}(\mathbf{x}) := \frac{\|\mathbf{x}_{\text{gt}} - \mathbf{x}\|^2}{\|\mathbf{x}_{\text{gt}}\|^2}, \quad \text{PSNR}(\mathbf{x}) := 20 \log_{10} \left(\frac{255}{\|\mathbf{x}_{\text{gt}} - \mathbf{x}\|} \right),$$

and by the structural similarity index (SSIM) [50]. Finally, all the numerical tests are replicable and the codes can be downloaded from [1].

6.1. Example 1: COULE. In this first example, we tested our proposal on an image of the COULE test set corrupted with some white Gaussian noise with level intensity of 2%. Regarding the parameter selection for the edge-weight function in (2.3), we chose $R = 5$ and $\sigma = 10^{-3}$.

The quality of the reconstructions achieved with different operators Ψ is presented in Table 6.1. Specifically, the upper part of the table displays the values of the initial reconstructions while the lower part displays the values obtained by **graphLa+ Ψ** combined with the corresponding initial reconstructor Ψ .

Notably, the **graphLa+ Ψ** method results in a substantially greater improvement across all metrics for all initial reconstructors Ψ , with the highest performance attained by **graphLa+Net**.

Initial reconstructors Ψ	RRE	SSIM	PSNR
FBP	0.0761	0.2219	22.3671
Tik	0.0478	0.4607	24.4129
TV	0.0328	0.8275	29.6926
Net	0.0164	0.9461	35.6828
graphLa+ Ψ			
graphLa+FBP	0.0279	0.7594	31.0908
graphLa+Tik	0.0272	0.9380	31.3000
graphLa+TV	0.0162	0.9822	35.8047
graphLa+Net	0.0098	0.9844	40.1793
graphLa+ \mathbf{x}_{gt}	0.0043	0.9866	47.2474

TABLE 6.1

Quality of initial and final reconstruction for different Ψ for the COULE dataset.

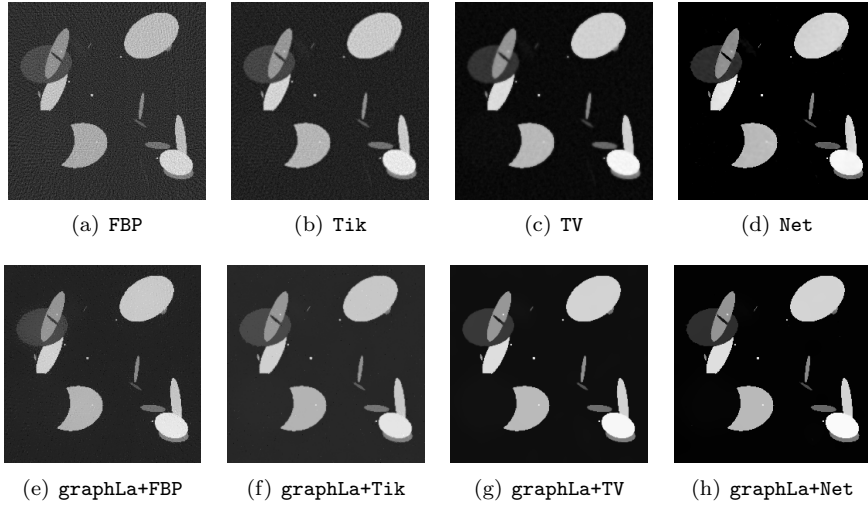


FIG. 6.1. Initial and final reconstructions using graphLa+ Ψ method for different Ψ .

As further confirmation, Figure 6.1 displays the reconstructions obtained for different Ψ . The level of details and sharpness in the graphLa+Net image is incomparable with all the other methods.

As a final investigation into the capabilities of our proposal, we tested the stability of the method against varying noise intensity. In Figure 6.2, we present the PSNR and SSIM values for various levels of noise. Similar to the previous analysis, the purple line represents the reconstruction obtained by utilizing the true image \mathbf{x}_{gt} to compute the graph Laplacian. Notably, even though our neural network was trained with a 0% noise level, the graphLa+Net method consistently outperforms all other cases across all noise levels. Additionally, Figure 6.2 shows that the integration of the graph Laplacian with the DNN serves as an effective regularization method, in contrast to the standalone application of the DNN.

6.2. Example 2: Mayo. In this second example, we tested our proposal on an image of the Mayo test set corrupted with some white Gaussian noise. Regarding the parameter selection for the edge-weight function in (2.3), we chose $R = 5$ and

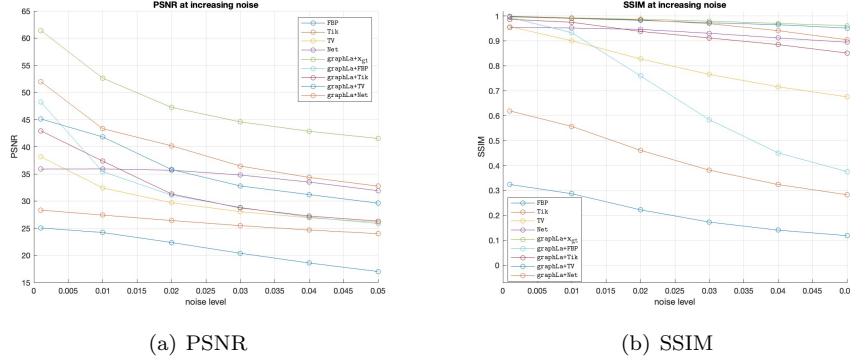


FIG. 6.2. *PSNR and SSIM for different level of noises and different reconstructors Ψ for the COULE dataset.*

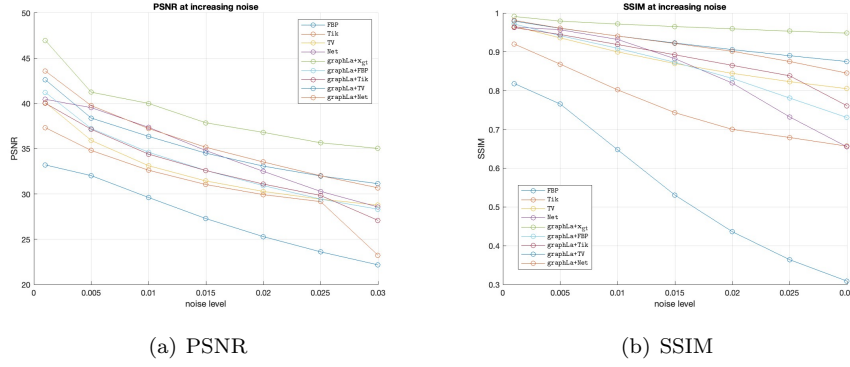


FIG. 6.3. *PSNR and SSIM for different level of noises and different reconstructors Ψ for the Mayo dataset*

$\sigma = 2 \times 10^{-4}$, except for the **graphLa+Net** method for which we used $R = 3$ and $\sigma = 10^{-3}$.

Given that the Mayo dataset reflects a real-world scenario, the ground truth images \mathbf{x}_{gt} , used for generating sinograms and for comparison, are not the actual true images. Instead, they are reconstructions themselves, inherently containing some level of noise. Consequently, comparing metrics for a fixed level of additional noise, as done in Table 6.1, is a bit less informative. Instead, it is still interesting to evaluate the **graphLa+ Ψ** method across different reconstructors Ψ and various levels of noise intensity using both PSNR and SSIM metrics, see Figure 6.3. As previously noted in the COULE example, the **graphLa+Net** method consistently outperforms all other cases, even if the neural network was trained with a 0% noise level.

In Figure 6.4, we present a visual inspection of some of the reconstructions for $\delta = 1\%$. Notably, the **graphLa+Net** image exhibits the sharpest quality compared to all other cases, and being very close to the upper limit given by **graphLa+ x_{gt}** .

As additional confirmation, in Figure 6.5 we zoom on the central part of the considered image. In this way, we can clearly note that the **graphLa+Net** approach achieves also an extraordinary quality of detail in the reconstruction.

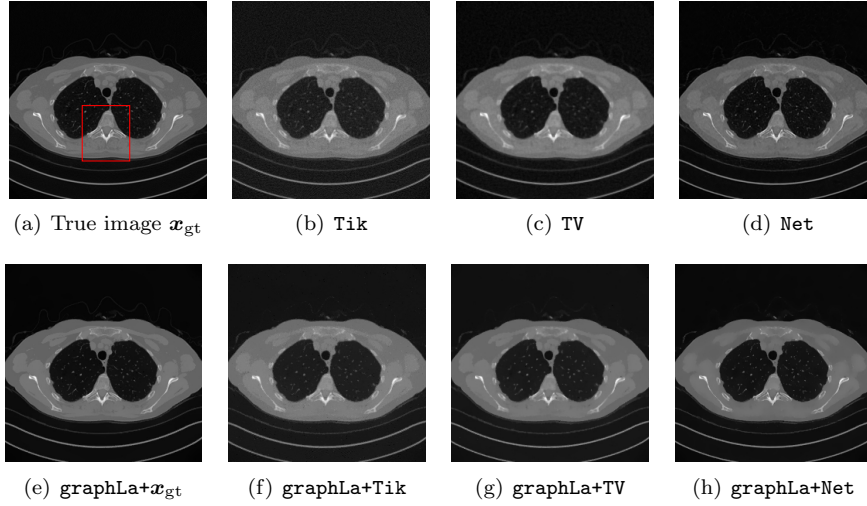
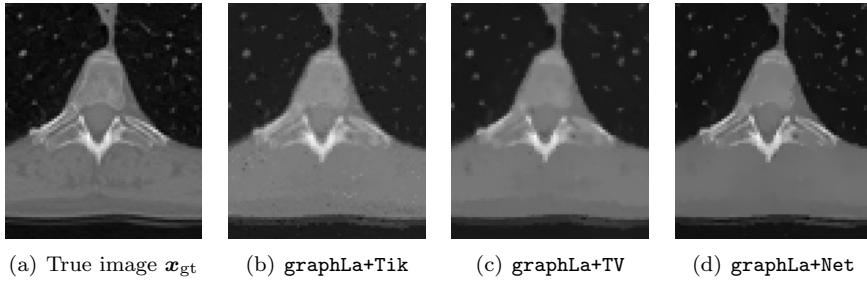

 FIG. 6.4. Initial and final reconstructions using graphLa+ Ψ method for different Ψ .


FIG. 6.5. Zoom in of the central lower part for different methods.

7. Conclusions. In this work we introduced and analyzed a novel regularization method which uses a graph Laplacian operator built upon a first approximation of the solution through a reconstructor Ψ . We demonstrated that under certain, albeit very weak, hypotheses on the reconstructor Ψ , **graphLa+ Ψ** is a convergent and stable regularization method. In all the proposed numerical examples, **graphLa+ Ψ** greatly enhanced the quality of the reconstructions for every initial reconstructor Ψ .

Moreover, leveraging the regularization property of **graphLa+ Ψ** , we suggested to use a DNN as first reconstructor Ψ . This new hybrid method, called **graphLa+Net**, merges the regularity of a standard variational method and the accuracy of a DNN, giving as a result a stable regularization method with very high accuracy.

In forthcoming works we will focus more on sharpening the choices for the edge-weight function $w_{\mathbf{x}}$ such as building an automatic rule for estimating its parameters.

Appendix A. Theoretical analysis. In this appendix we collect the proofs of the results presented in [Subsection 3.1](#). We will assume that all the hypotheses introduced so far are satisfied, i.e. [Hypotheses 2.1, 3.1, 3.6, 3.8, and 3.9](#).

We begin with the invariance property of the null space of the graph Laplacians built upon Ψ_{Θ}^{δ} .

Lemma 3.7.

Proof. The null space of a generic graph Laplacian, as per [Definition 2.3](#), is given by the subspace of functions which are constant on the connected components of the node set P . By [Hypothesis 3.6](#), it is easy to check that a sequence $\{p_i\}_{i=0}^k$ is a walk with respect to $w_{\Psi_\Theta^\delta}$ if and only if it is a walk with respect to w_0 . Therefore, all the connected components of P , identified by $w_{\Psi_\Theta^\delta}$ and w_0 , are invariant. This concludes the proof. \square

A.1. Existence of solutions and well-posedness of graphLa+ Ψ . Define

$$(A.1) \quad \Gamma(\mathbf{x}) := \frac{1}{2} \|K\mathbf{x} - \mathbf{y}^\delta\|_2^2 + \alpha \|\Delta_{\Psi_\Theta^\delta} \mathbf{x}\|_1.$$

We recall that a (nonnegative) functional $\Gamma: X \rightarrow [0, \infty)$ is *coercive* if $\Gamma(\mathbf{x}) \rightarrow \infty$ for $\|\mathbf{x}\| \rightarrow \infty$, where $\|\cdot\|$ can be any norm on $X \simeq \mathbb{R}^n$.

Thanks to [Hypothesis 3.8](#), the functional (A.1) is coercive, for every fixed $\alpha > 0$ and $\delta \geq 0$. Although this should certainly be well-known, for the convenience of the reader we include a short proof in the next lemma.

LEMMA A.1. Γ is coercive for every fixed $\alpha > 0$ and $\delta \geq 0$.

Proof. Let V be the invariant null space of $\Delta_{\Psi_\Theta^\delta}$ from [Lemma 3.7](#), and let us indicate with π and π_\perp the projection into V and V^\perp , respectively. In general, it holds that

$$(A.2) \quad \inf_{\substack{\mathbf{u} \in V^\perp \\ \mathbf{u} \neq \mathbf{0}}} \frac{\|\Delta_{\Psi_\Theta^\delta} \mathbf{u}\|_1}{\|\mathbf{u}\|_1} \geq \gamma_1 > 0.$$

Since $\ker(K) \cap V = \{\mathbf{0}\}$ by [Hypothesis 3.8](#), then it holds that too

$$(A.3) \quad \inf_{\substack{\mathbf{v} \in V \\ \mathbf{v} \neq \mathbf{0}}} \frac{\|K\mathbf{v}\|_2}{\|\mathbf{v}\|_2} \geq \gamma_2 > 0.$$

Fix a sequence $\{\mathbf{x}_j\}$ such that $\|\mathbf{x}_j\|_2 \rightarrow \infty$. We want to show that $\Gamma(\mathbf{x}_j) \rightarrow \infty$. Clearly, for $j \rightarrow \infty$

$$\|\mathbf{x}_j\|_2 \rightarrow \infty \quad \text{if and only if} \quad \|\pi \mathbf{x}_j\|_2^2 + \|\pi_\perp \mathbf{x}_j\|_1 \rightarrow \infty.$$

There are two cases:

- (i) $\lim_j \|\pi_\perp \mathbf{x}_j\|_1 = \infty$;
- (ii) $\liminf_j \|\pi_\perp \mathbf{x}_j\|_1 \leq c < \infty$ and $\lim_j \|\pi \mathbf{x}_j\|_2^2 = \infty$.

If we are in (i), then by (A.2)

$$(A.4) \quad \begin{aligned} \alpha \gamma_1 \|\pi_\perp \mathbf{x}_j\|_1 &\leq \alpha \|\Delta_{\Psi_\Theta^\delta} \pi_\perp \mathbf{x}_j\|_1 \\ &\leq \frac{1}{2} \|K\mathbf{x}_j - \mathbf{y}^\delta\|_2^2 + \alpha \|\Delta_{\Psi_\Theta^\delta} \mathbf{x}_j\|_1 = \Gamma(\mathbf{x}_j). \end{aligned}$$

If we are in (ii), then by (A.3)

$$(A.5) \quad \begin{aligned} \frac{\gamma_2}{4} \|\pi \mathbf{x}_j\|_2^2 &\leq \frac{1}{4} \|K\pi \mathbf{x}_j\|_2^2 \leq \frac{1}{2} \|K\mathbf{x}_j - \mathbf{y}^\delta\|_2^2 + \alpha \|\Delta_{\Psi_\Theta^\delta} \mathbf{x}_j\|_1 + \frac{1}{2} \|K\pi_\perp \mathbf{x}_j - \mathbf{y}^\delta\|_2^2 \\ &= \Gamma(\mathbf{x}_j) + \frac{1}{2} \|K\pi_\perp \mathbf{x}_j - \mathbf{y}^\delta\|_2^2. \end{aligned}$$

Notice that from (ii) it follows that $\liminf_j \|K\pi_\perp \mathbf{x}_j - \mathbf{y}^\delta\|_2^2$ is bounded.

Passing to the \liminf in both (A.4) and (A.5) we conclude. \square

Remark A.2. The same result as in [Lemma A.1](#) applies when replacing Ψ_Θ^δ with \mathbf{x}_0 in Γ , and the proof remains unchanged.

Proposition 3.10.

Proof. The existence relies on standard topological arguments, but we provide a comprehensive exposition for the convenience of the reader.

Let

$$c := \inf\{\|\Delta_{\mathbf{x}_0}\mathbf{x}\|_1 \mid \mathbf{x} \in X, K\mathbf{x} = \mathbf{y}\},$$

which is well-defined thanks to [Hypothesis 2.1](#). Therefore there exists a sequence $\{\mathbf{x}_j\}$ such that $K\mathbf{x}_j = \mathbf{y}$ for every j and $\lim_j \|\Delta_{\mathbf{x}_0}\mathbf{x}_j\|_1 = c$. In particular, there exists $c_1 > 0$ such that

$$(A.6) \quad \|\Delta_{\mathbf{x}_0}\mathbf{x}_j\|_1 \leq c_1 \quad \text{for every } j.$$

There are two possible cases:

- (i) $\|\mathbf{x}_j\|_2 \leq c_2$ for some $c_2 > 0$, for every j ;
- (ii) There exists a subsequence $\{\mathbf{x}_{j'}\}$, such that $\lim_{j'} \|\mathbf{x}_{j'}\|_2 = \infty$.

If we are in case (i), then by compactness and continuity arguments we can conclude that there exists \mathbf{x}_{sol} such that

$$\lim_{j'} \mathbf{x}_{j'} = \mathbf{x}_{\text{sol}}, \quad \text{and} \quad \begin{cases} K\mathbf{x}_{\text{sol}} = \mathbf{y}, \\ \|\Delta_{\mathbf{x}_0}\mathbf{x}_{\text{sol}}\|_1 = c, \end{cases}$$

that is, \mathbf{x}_{sol} is a graph-minimizing solution with respect to \mathbf{x}_0 .

Suppose now we are in case (ii). By [Lemma A.1](#) and [Remark A.2](#), $\Gamma(\mathbf{x}_{j'}) \rightarrow \infty$ for any fixed α, δ . Since $\|K\mathbf{x}_{j'} - \mathbf{y}^\delta\|_2^2 = \|\mathbf{y} - \mathbf{y}^\delta\|_2^2 \leq \delta^2$ for every j' , it follows necessarily that $\lim_{j'} \|\Delta_{\mathbf{x}_0}\mathbf{x}_{j'}\|_1 = \infty$. This leads to an absurdity in light of (A.6). \square

Proposition 3.11.

Proof. From [Lemma A.1](#), the nonnegative functional Γ is coercive on a finite dimensional vector space. By standard theory, there exists a minimizer, see for example [6, Proposition 11.15]. \square

Corollary 3.12.

Proof. The uniqueness of \mathbf{x}_{sol} is straightforward. On the other hand, the uniqueness of $\mathbf{x}_{\Psi_\Theta^\delta, \alpha}^\delta$ is derived from the fact that if K is injective then the functional $\mathbf{x} \mapsto \|K\mathbf{x} - \mathbf{y}^\delta\|_2^2$ is strongly convex. This property leads to the strong (and therefore strict) convexity of Γ . According to [6, Corollary 11.9], the desired result follows. \square

A.2. Convergence and stability analysis. In this subsection we prove [Theorems 3.14](#) and [3.15](#). The main difficulty is given by the regularization term $\mathcal{R}(\mathbf{x}, \mathbf{y}^\delta)$, that depends on the observed data \mathbf{y}^δ . Therefore, all standard techniques can not be applied straightforwardly.

A crucial role will be played by the following two lemmas, which guarantee uniform convergence of $\Delta_{\Psi_\Theta^\delta}$, and a special uniform coercivity property for Γ in (A.1).

LEMMA A.3. *Let $\Theta = \Theta(\delta, \mathbf{y}^\delta)$, \mathbf{x}_0 and g be defined as in [Hypothesis 3.1](#). For every $\mathbf{x} \in X$ it holds that*

$$\|\Delta_{\Psi_\Theta^\delta}\mathbf{x} - \Delta_{\mathbf{x}_0}\mathbf{x}\|_1 \leq c\|\mathbf{x}\|_\infty g(\delta, \mathbf{x}_0) \rightarrow 0 \quad \text{as } \delta \rightarrow 0,$$

where c is a positive constant independent of \mathbf{x} . In particular, the convergence is uniform on every compact subset.

Proof. We use the notations introduced in [Subsections 2.1.1](#) and [3.1](#). In particular, $w_{\Psi_\Theta^\delta}$ and w_0 are the edge-weight functions in [\(2.1\)](#) induced by $\Psi_\Theta^\delta := \Psi_\Theta(\mathbf{y}^\delta)$ and \mathbf{x}_0 , respectively; $\mu_{\Psi_\Theta^\delta}$ and μ_0 are the node measures in [\(2.2\)](#) induced by Ψ_Θ^δ and \mathbf{x}_0 , respectively. Let us observe that, with this notation, [Hypothesis 3.1](#) now reads

$$\|\Psi_\Theta^\delta - \mathbf{x}_0\|_2 \leq g(\delta, \mathbf{x}_0) \quad \text{as } \delta \rightarrow 0.$$

Define

$$t_{\delta,p,q} := |\Psi_\Theta^\delta(p) - \Psi_\Theta^\delta(q)|, \quad t_{0,p,q} := |\mathbf{x}_0(p) - \mathbf{x}_0(q)|, \quad d := \max_{p,q} \{w_d(p, q)\}.$$

Then,

$$\begin{aligned} |\Delta_{\Psi_\Theta^\delta} \mathbf{x}(p) - \Delta_{\mathbf{x}_0} \mathbf{x}(p)| &\leq \sum_{q \in P} \left| \frac{w_{\Psi_\Theta^\delta}(p, q)}{\mu_{\Psi_\Theta^\delta}(p)} - \frac{w_0(p, q)}{\mu_0(p)} \right| |\mathbf{x}(p) - \mathbf{x}(q)| \\ &= \sum_{q \in P} w_d(p, q) \left| \frac{h_i(t_{\delta,p,q})}{\mu_{\Psi_\Theta^\delta}(p)} - \frac{h_i(t_{0,p,q})}{\mu_0(p)} \right| |\mathbf{x}(p) - \mathbf{x}(q)| \\ (A.7) \quad &\leq \frac{2d \|\mathbf{x}\|_\infty}{\mu_{\Psi_\Theta^\delta}(p) \mu_0(p)} \sum_{q \in P} \left| \mu_0(p) h_i(t_{\delta,p,q}) - \mu_{\Psi_\Theta^\delta}(p) h_i(t_{0,p,q}) \right|. \end{aligned}$$

We need to bound the right-hand side of the last inequality. Because of the locally Lipschitz continuity of the maps h_i and $\Psi_\Theta^\delta \mapsto \mu_{\Psi_\Theta^\delta}(p)$, granted by [Hypothesis 3.9](#), then for δ small enough there exists a positive constant \bar{c} , independent of p , such that

$$\frac{2d}{\mu_{\Psi_\Theta^\delta}(p) \mu_0(p)} \leq \bar{c}, \quad |\mu_{\Psi_\Theta^\delta}(p) - \mu_0(p)| \leq \bar{c} \|\Psi_\Theta^\delta - \mathbf{x}_0\|_2, \quad \text{and} \quad |h_i(t_{\delta,p,q}) - h_i(t_{0,p,q})| \leq \bar{c} |t_{\delta,p,q} - t_{0,p,q}|.$$

Therefore, by adding and subtracting the auxiliary term $\mu_0(p) h_i(t_{0,p,q})$, it holds that

$$\begin{aligned} (A.8) \quad & \left| \mu_0(p) h_i(t_{\delta,p,q}) - \mu_{\Psi_\Theta^\delta}(p) h_i(t_{0,p,q}) \right| \leq \mu_0(p) |h_i(t_{\delta,p,q}) - h_i(t_{0,p,q})| + |\mu_{\Psi_\Theta^\delta}(p) - \mu_0(p)| h_i(t_{0,p,q}) \\ & \leq \bar{c} \mu_0(p) |t_{\delta,p,q} - t_{0,p,q}| + \bar{c} \|\Psi_\Theta^\delta - \mathbf{x}_0\|_2 h_i(t_{0,p,q}) \\ & \leq \bar{c} \max_p \{\mu_0(p)\} |t_{\delta,p,q} - t_{0,p,q}| + \bar{c} \max_{p,q} \{h_i(t_{0,p,q})\} g(\delta, \mathbf{x}_0). \end{aligned}$$

Let us bound now $|t_{\delta,p,q} - t_{0,p,q}|$:

$$\begin{aligned} (A.9) \quad & |t_{\delta,p,q} - t_{0,p,q}| = \left| |\Psi_\Theta^\delta(p) - \Psi_\Theta^\delta(q)| - |\mathbf{x}_0(p) - \mathbf{x}_0(q)| \right| \\ & \leq \left| (\Psi_\Theta^\delta(p) - \mathbf{x}_0(p)) + (\mathbf{x}_0(q) - \Psi_\Theta^\delta(q)) \right| \\ & \leq |\Psi_\Theta^\delta(p) - \mathbf{x}_0(p)| + |\Psi_\Theta^\delta(q) - \mathbf{x}_0(q)| \\ & \leq 2\sqrt{n} \|\Psi_\Theta^\delta - \mathbf{x}_0\|_2 \leq 2\sqrt{n} g(\delta, \mathbf{x}_0). \end{aligned}$$

Combining [\(A.7\)](#)–[\(A.9\)](#), we get that

$$|\Delta_{\Psi_\Theta^\delta} \mathbf{x}(p) - \Delta_{\mathbf{x}_0} \mathbf{x}(p)| \leq n \bar{c}^2 \left(2\sqrt{n} \max_p \{\mu_0(p)\} + \max_{p,q} \{h_i(t_{0,p,q})\} \right) \|\mathbf{x}\|_\infty g(\delta, \mathbf{x}_0),$$

and then the thesis easily follows. \square

Let us point out that the constants that appears in the proof depends on the dimension n . Appropriate choices of w_d , h_i and $\mu_{\mathbf{x}}$, with respect to n , could make c independent of n itself. However, there is still the issue of the convergence of the (sequence of) graph Laplacians $\Delta_{\mathbf{x}}$ as $n \rightarrow \infty$, and this is beyond the scope of this work.

LEMMA A.4. *Let $\Theta = \Theta(\delta, \mathbf{y}^\delta)$ be the parameter choice rule as in [Hypothesis 3.1](#) and let $\delta_k \rightarrow 0$. Write $\Theta_k := \Theta(\delta_k, \mathbf{y}^{\delta_k})$ and fix $\alpha > 0$. For any sequence $\{\mathbf{x}_k\}$ such that $\limsup_k \|\mathbf{x}_k\|_2 = \infty$, then*

$$\limsup_k \frac{1}{2} \|K\mathbf{x}_k - \mathbf{y}\|_2^2 + \alpha \|\Delta_{\Psi_{\Theta_k}^{\delta_k}} \mathbf{x}_k\|_1 = \infty.$$

Proof. Let V be the invariant null space from [Lemma 3.7](#). Define

$$\gamma_k := \inf_{\substack{\mathbf{u} \in V^\perp \\ \|\mathbf{u}\|_1=1}} \|\Delta_{\Psi_{\Theta_k}^{\delta_k}} \mathbf{u}\|_1 \quad \text{and} \quad \gamma_0 := \inf_{\substack{\mathbf{u} \in V^\perp \\ \|\mathbf{u}\|_1=1}} \|\Delta_{\mathbf{x}_0} \mathbf{u}\|_1 > 0.$$

By [Lemma A.3](#) and uniform convergence on compact sets, it holds that

$$\forall \mathbf{u} \in V^\perp \text{ s.t. } \|\mathbf{u}\|_1 = 1, \quad \|\Delta_{\mathbf{x}_0} \mathbf{u}\|_1 - \frac{\gamma_0}{2} \leq \|\Delta_{\Psi_{\Theta_k}^{\delta_k}} \mathbf{u}\|_1 \quad \text{for } k \geq N = N(\gamma_0).$$

Therefore,

$$\inf_{\substack{\mathbf{u} \in V^\perp \\ \|\mathbf{u}\|_1=1}} \|\Delta_{\Psi_{\Theta_k}^{\delta_k}} \mathbf{u}\|_1 \geq \frac{\gamma_0}{2} \quad \forall k \geq N(\gamma_0).$$

In particular, there exists $\gamma_1 > 0$ such that

$$\|\Delta_{\Psi_{\Theta_k}^{\delta_k}} \mathbf{x}\|_1 \geq \gamma_1 \|\pi_\perp \mathbf{x}\|_1 \quad \forall \mathbf{x}, \forall k.$$

The rest of the proof follows like in [Lemma A.1](#). \square

The next theorem presents a convergence result for the **graphLa+Ψ** method [\(3.1\)](#). The overall proof follows a fairly standard approach, as for example in [\[47, Theorem 3.26\]](#). However, since the regularizing term in [\(3.1\)](#) depends on the data \mathbf{y}^δ as well, it involves a few nontrivial technical aspects.

We will use a slight modification of the notation introduced in [\(A.1\)](#). Specifically,

$$\Gamma_k(\mathbf{x}) := \frac{1}{2} \|K\mathbf{x} - \mathbf{y}^{\delta_k}\|_2^2 + \alpha_k \|\Delta_{\Psi_{\Theta_k}^{\delta_k}} \mathbf{x}\|_1.$$

Theorem 3.14.

Proof. The sequence $\{\mathbf{x}_k\}$ is well-posed thanks to [Proposition 3.11](#). Fix a graph-minimizing solution \mathbf{x}_{sol} as in [Definition 3.5](#), which exists because of [Proposition 3.10](#). Then, by definition, it holds that

$$(A.10) \quad \Gamma_k(\mathbf{x}_k) \leq \Gamma_k(\mathbf{x}_{\text{sol}}) \leq \frac{\delta_k^2}{2} + \alpha_k \|\Delta_{\mathbf{x}_0} \mathbf{x}_{\text{sol}}\|_1 + \alpha_k c \|\mathbf{x}_{\text{sol}}\|_\infty g(\delta_k, \mathbf{x}_0) \rightarrow 0$$

as $\delta \rightarrow 0$, where the last inequality comes from [Lemma A.3](#), and the convergence to zero is granted by [\(3.4a\)](#). Therefore, $\|K\mathbf{x}_k - \mathbf{y}^{\delta_k}\|_2^2 \rightarrow 0$, and in particular

$$(A.11) \quad \|K\mathbf{x}_k - \mathbf{y}\|_2 \leq \|K\mathbf{x}_k - \mathbf{y}^{\delta_k}\|_2 + \delta_k \rightarrow 0 \quad \text{as } \delta_k \rightarrow 0.$$

Since

$$\alpha_k \|\Delta_{\Psi_{\Theta_k}^{\delta_k}} \mathbf{x}_k\|_1 \leq \Gamma_k(\mathbf{x}_k),$$

then by (3.4b) and (A.10), we get that

$$(A.12) \quad \limsup_k \|\Delta_{\Psi_{\Theta_k}^{\delta_k}} \mathbf{x}_k\|_1 \leq \|\Delta_{\mathbf{x}_0} \mathbf{x}_{\text{sol}}\|_1.$$

Let $\alpha^+ := \max\{\alpha_k \mid k \in \mathbb{N}\}$. Then, combining (A.11) and (A.12),

$$\frac{1}{2} \|K\mathbf{x}_k - \mathbf{y}\|_2^2 + \alpha^+ \|\Delta_{\Psi_{\Theta_k}^{\delta_k}} \mathbf{x}_k\|_1 \leq c < \infty,$$

and from Lemma A.4 we deduce that $\{\mathbf{x}_k\}$ is bounded. Therefore, there exists a convergent subsequence $\{\mathbf{x}_{k'}\}$ which converges to a point \mathbf{x}^* . From (A.11), it holds that $K\mathbf{x}^* = \mathbf{y}$. Moreover, by the boundedness of $\{\mathbf{x}_{k'}\}$ and the uniform convergence granted by Lemma A.3, we infer that

$$\|\Delta_{\mathbf{x}_0} \mathbf{x}^*\|_1 = \lim_{k'} \|\Delta_{\Psi_{\Theta_{k'}}^{\delta_{k'}}} \mathbf{x}_{k'}\|_1.$$

Applying (A.12), we finally get

$$\|\Delta_{\mathbf{x}_0} \mathbf{x}^*\|_1 = \lim_{k'} \|\Delta_{\Psi_{\Theta_{k'}}^{\delta_{k'}}} \mathbf{x}_{k'}\|_1 \leq \|\Delta_{\mathbf{x}_0} \mathbf{x}_{\text{sol}}\|_1 \leq \|\Delta_{\mathbf{x}_0} \mathbf{x}^*\|_1.$$

That is, \mathbf{x}^* is a graph-minimizing solution. If the graph-minimization solution is unique, then we have just proven that every subsequence of $\{\mathbf{x}_k\}$ has a subsequence converging to \mathbf{x}_{sol} , and therefore $\mathbf{x}_k \rightarrow \mathbf{x}_{\text{sol}}$ by a standard topological argument. \square

We proceed now to prove the stability result in Theorem 3.15. However, as first step we demonstrate that the standard Tikhonov reconstruction method coupled with the discrepancy principle satisfies Hypothesis 3.2.

EXAMPLE A.5. Consider a standard Tikhonov reconstruction method, that is

$$\Psi_{\Theta}(\mathbf{y}) := (K^T K + \Theta I)^{-1} K^T \mathbf{y},$$

where $\Theta \in (0, \infty)$. Let $\Theta = \Theta(\delta, \mathbf{y}^\delta)$ defined by the discrepancy principle as per [21, Equation (4.57)]. Then it is easy to check that $\Theta_k \rightarrow \Theta = \Theta(\delta, \mathbf{y}^\delta)$ for $k \rightarrow \infty$. Setting

$$\mathcal{T}^k = (K^T K + \Theta_k I)^{-1} \quad \text{and} \quad \mathcal{T} = (K^T K + \Theta I)^{-1},$$

it holds that

$$\|\Psi_{\Theta_k}(\mathbf{y}^{\delta_k}) - \Psi_{\Theta}(\mathbf{y}^\delta)\|_2 \leq \underbrace{\|(\mathcal{T}^k - \mathcal{T})K^T \mathbf{y}^{\delta_k}\|_2}_{\text{I}} + \underbrace{\|\mathcal{T}K^T(\mathbf{y}^\delta - \mathbf{y}^{\delta_k})\|_2}_{\text{II}}.$$

Now,

$$\text{I} \leq |\Theta - \Theta_k| \|\mathcal{T}^k\| \|\mathcal{T}K^T\| \|\mathbf{y}^{\delta_k}\|_2 \leq \frac{|\Theta - \Theta_k|}{2\Theta_k \sqrt{\Theta}} \|\mathbf{y}^{\delta_k}\|_2 = f_1(k) \rightarrow 0,$$

and

$$\text{II} \leq \|(K^T K + \Theta I)^{-1} K^T\| \|\mathbf{y}^\delta - \mathbf{y}^{\delta_k}\|_2 \leq \frac{1}{2\sqrt{\Theta}} \|\mathbf{y}^\delta - \mathbf{y}^{\delta_k}\|_2 = f_2(k) \rightarrow 0.$$

Now we need a couple of preliminary lemmas.

LEMMA A.6. *For all $\mathbf{x} \in X$ and $\mathbf{y}^{\delta_{k_1}}, \mathbf{y}^{\delta_{k_2}} \in Y$, we have*

$$\Gamma_{k_1}(\mathbf{x}) \leq 2\Gamma_{k_2}(\mathbf{x}) + \|\mathbf{y}^{\delta_{k_1}} - \mathbf{y}^{\delta_{k_2}}\| + \|(\Delta_{\Psi_{\Theta_{k_1}}}^{\delta_{k_1}} - \Delta_{\Psi_{\Theta_{k_2}}}^{\delta_{k_2}})\mathbf{x}\|_1$$

Proof. By standard p -norm inequalities

$$\begin{aligned} \Gamma_{k_1}(\mathbf{x}) &= \frac{1}{2}\|K\mathbf{x} - \mathbf{y}^{\delta_{k_1}}\|_2^2 + \alpha\|\Delta_{\Psi_{\Theta_{k_1}}}^{\delta_{k_1}}\mathbf{x}\|_1 \\ &\leq \|K\mathbf{x} - \mathbf{y}^{\delta_{k_2}}\|_2^2 + \|\mathbf{y}^{\delta_{k_1}} - \mathbf{y}^{\delta_{k_2}}\|_2^2 + \alpha\|\Delta_{\Psi_{\Theta_{k_1}}}^{\delta_{k_1}}\mathbf{x}\|_1 \\ &\leq 2\Gamma_{k_2}(\mathbf{x}) + \|\mathbf{y}^{\delta_{k_1}} - \mathbf{y}^{\delta_{k_2}}\| + \|(\Delta_{\Psi_{\Theta_{k_1}}}^{\delta_{k_1}} - \Delta_{\Psi_{\Theta_{k_2}}}^{\delta_{k_2}})\mathbf{x}\|_1 \quad \square \end{aligned}$$

LEMMA A.7. *Let δ_k , Θ_k , Θ and f defined as in Hypothesis 3.2. It holds that*

$$\|\Delta_{\Psi_{\Theta_k}}^{\delta_k}\mathbf{x} - \Delta_{\Psi_{\Theta}}^{\delta}\mathbf{x}\|_1 \leq c\|\mathbf{x}\|_{\infty}f(k) \rightarrow 0 \quad \text{as } k \rightarrow \infty,$$

where c is a positive constant independent of \mathbf{x} .

Proof. The proof is similar to Lemma A.3 using hypothesis 3.2. \square

Theorem 3.15.

Proof. Because \mathbf{x}_k is a minimizer of Γ_k , we have

$$(A.13) \quad \Gamma_k(\mathbf{x}_k) \leq \Gamma_k(\mathbf{x}), \quad \forall \mathbf{x} \in X.$$

Choose now a vector $\bar{\mathbf{x}} \in X$. By applying the previous equation to $\mathbf{x} = \bar{\mathbf{x}}$ and using twice Lemma A.6, it follows that

$$\begin{aligned} \Gamma(\mathbf{x}_k) &\leq 2\Gamma_k(\mathbf{x}_k) + \|\mathbf{y}^{\delta} - \mathbf{y}^{\delta_k}\| + \|(\Delta_{\Psi_{\Theta}}^{\delta} - \Delta_{\Psi_{\Theta_k}}^{\delta_k})\mathbf{x}_k\|_1 \\ &\leq 2\Gamma_k(\bar{\mathbf{x}}) + \|\mathbf{y}^{\delta} - \mathbf{y}^{\delta_k}\| + \|(\Delta_{\Psi_{\Theta}}^{\delta} - \Delta_{\Psi_{\Theta_k}}^{\delta_k})\mathbf{x}_k\|_1 \\ &\leq 4\Gamma(\bar{\mathbf{x}}) + 2\|\mathbf{y}^{\delta} - \mathbf{y}^{\delta_k}\| + 2\|(\Delta_{\Psi_{\Theta}}^{\delta} - \Delta_{\Psi_{\Theta_k}}^{\delta_k})\mathbf{x}_k\|_1. \end{aligned}$$

From Lemma A.7, since \mathbf{y}^{δ_k} converges to \mathbf{y}^{δ} with respect to the norm topology, then there exist $k_0 \in \mathbb{N}$ such that \square

$$M := 2\Gamma(\bar{\mathbf{x}}) + 1 \geq \Gamma(\mathbf{x}_k), \quad \forall k \geq k_0.$$

The thesis now follows easily by adapting the proof in [47, Theorem 3.4].

REFERENCES

- [1] S. ALEOTTI, D. BIANCHI, D. EVANGELISTA, M. DONATELLI, AND E. LOLI PICCOLOMINI, *Official GitHub repository for the graphla+ ψ codes*, 2023, <https://github.com/devangelista2/GraphLaPlus>. Online; accessed 22-December-2023.
- [2] A. ALI AND R. J. TIBSHIRANI, *The Generalized Lasso Problem and Uniqueness*, Electronic Journal of Statistics, 13 (2019), pp. 2307–2347.
- [3] V. ANTUN, F. RENNA, C. POON, B. ADCOCK, AND A. C. HANSEN, *On instabilities of deep learning in image reconstruction and the potential costs of AI*, in Proceedings of the National Academy of Sciences, vol. 117, 2020, pp. 30088–30095.

- [4] P. ARIAS, V. CASELLES, AND G. SAPIRO, *A variational framework for non-local image inpainting*, in International Workshop on Energy Minimization Methods in Computer Vision and Pattern Recognition, Springer, 2009, pp. 345–358.
- [5] S. ARRIDGE, P. MAASS, O. ÖKTEM, AND C.-B. SCHÖNLIEB, *Solving inverse problems using data-driven models*, Acta Numerica, 28 (2019), pp. 1–174.
- [6] H. H. BAUSCHKE AND P. L. COMBETTES, *Convex Analysis and Monotone Operator Theory in Hilbert Spaces*, CMS books in mathematics, Springer Cham, 2 ed., 2017.
- [7] D. BIANCHI, A. BUCCINI, M. DONATELLI, AND E. RANDAZZO, *Graph Laplacian for image deblurring*, ETNA, 55 (2022), pp. 169–186.
- [8] D. BIANCHI, A. BUCCINI, M. DONATELLI, AND S. SERRA-CAPIZZANO, *Iterated fractional Tikhonov regularization*, Inverse Problems, 31 (2015), p. 055005.
- [9] D. BIANCHI AND M. DONATELLI, *On generalized iterated Tikhonov regularization with operator-dependent seminorms*, Electronic Transactions on Numerical Analysis, 47 (2017), pp. 73–99.
- [10] D. BIANCHI AND M. DONATELLI, *Graph approximation and generalized Tikhonov regularization for signal deblurring*, in 2021 21st International Conference on Computational Science and Its Applications (ICCSA), IEEE, 2021, pp. 93–100.
- [11] D. BIANCHI, M. DONATELLI, D. EVANGELISTA, W. LI, AND E. L. PICCOLOMINI, *Graph Laplacian and Neural Networks for Inverse Problems in Imaging: GraphLaNet*, in International Conference on Scale Space and Variational Methods in Computer Vision, 2023, pp. 175–186.
- [12] D. BIANCHI, G. LAI, AND W. LI, *Uniformly convex neural networks and non-stationary iterated network Tikhonov (iNETT) method*, Inverse Problems, 39 (2023), p. 055002.
- [13] M. M. BRONSTEIN, J. BRUNA, Y. LECUN, A. SZLAM, AND P. VANDERGHEYNST, *Geometric Deep Learning: Going beyond Euclidean data*, IEEE Signal Processing Magazine, 34 (2017), pp. 18–42, <https://doi.org/10.1109/MSP.2017.2693418>.
- [14] A. BUCCINI AND M. DONATELLI, *Graph Laplacian in ℓ^2 – ℓ^q regularization for image reconstruction*, in 2021 21st International Conference on Computational Science and Its Applications (ICCSA), IEEE, 2021, pp. 29–38.
- [15] J.-F. CAI, R. H. CHAN, AND Z. SHEN, *A framelet-based image inpainting algorithm*, Applied and Computational Harmonic Analysis, 24 (2008), pp. 131–149.
- [16] Y. CAI, M. DONATELLI, D. BIANCHI, AND T.-Z. HUANG, *Regularization preconditioners for frame-based image deblurring with reduced boundary artifacts*, SIAM Journal on Scientific Computing, 38 (2016), pp. B164–B189.
- [17] L. CALATRONI, Y. VAN GENNIP, C.-B. SCHÖNLIEB, H. M. ROWLAND, AND A. FLENNER, *Graph clustering, variational image segmentation methods and Hough transform scale detection for object measurement in images*, Journal of Mathematical Imaging and Vision, 57 (2017), pp. 269–291.
- [18] E. CANDES AND B. RECHT, *Simple bounds for recovering low-complexity models*, Mathematical Programming, 141 (2013), pp. 577–589.
- [19] J. CHUNG AND S. GAZZOLA, *Flexible krylov methods for ℓ_p regularization*, SIAM Journal on Scientific Computing, 41 (2019), pp. S149–S171.
- [20] M. J. COLBROOK, V. ANTUN, AND A. C. HANSEN, *The difficulty of computing stable and accurate neural networks: On the barriers of deep learning and Smale’s 18th problem*, in Proceedings of the National Academy of Sciences, vol. 119, 2022, p. e2107151119.
- [21] H. W. ENGL, M. HANKE, AND A. NEUBAUER, *Regularization of inverse problems*, Springer Science & Business Media, 1996.
- [22] D. EVANGELISTA, E. MOROTTI, AND E. L. PICCOLOMINI, *COULE dataset*. <https://www.kaggle.com/datasets/loiboresearchgroup/coule-dataset>, 2023. Accessed on 01/12/2023.
- [23] D. EVANGELISTA, E. MOROTTI, AND E. L. PICCOLOMINI, *Rising: A new framework for model-based few-view ct image reconstruction with deep learning*, Computerized Medical Imaging and Graphics, 103 (2023), p. 102156.
- [24] S. GAZZOLA, P. C. HANSEN, AND J. G. NAGY, *Ir tools: a matlab package of iterative regularization methods and large-scale test problems*, Numerical Algorithms, 81 (2019), pp. 773–811.
- [25] G. GILBOA AND S. OSHER, *Nonlocal linear image regularization and supervised segmentation*, Multiscale Modeling & Simulation, 6 (2007), pp. 595–630.
- [26] G. GILBOA AND S. OSHER, *Nonlocal operators with applications to image processing*, Multiscale Modeling & Simulation, 7 (2009), pp. 1005–1028.
- [27] Y. S. HAN, J. YOO, AND J. C. YE, *Deep residual learning for compressed sensing CT reconstruction via persistent homology analysis*, arXiv preprint arXiv:1611.06391, (2016).
- [28] P. C. HANSEN, *Rank-deficient and discrete ill-posed problems: numerical aspects of linear inversion*, SIAM, 1998.

- [29] P. C. HANSEN, J. G. NAGY, AND D. P. O'LEARY, *Deblurring images: matrices, spectra, and filtering*, SIAM, 2006.
- [30] C. F. HIGHAM AND D. J. HIGHAM, *Deep learning: An introduction for applied mathematicians*, Siam review, 61 (2019), pp. 860–891.
- [31] M. E. HOCHSTENBACH AND L. REICHEL, *Fractional Tikhonov regularization for linear discrete ill-posed problems*, BIT Numerical Mathematics, 51 (2011), pp. 197–215.
- [32] J. HUANG, M. DONATELLI, AND R. H. CHAN, *Nonstationary iterated thresholding algorithms for image deblurring*, Inverse Probl. Imaging, 7 (2013), pp. 717–736.
- [33] K. H. JIN, M. T. MCCANN, E. FROUSTEY, AND M. UNSER, *Deep convolutional neural network for inverse problems in imaging*, IEEE transactions on image processing, 26 (2017), pp. 4509–4522.
- [34] A. C. KAK AND M. SLANEY, *Principles of computerized tomographic imaging*, SIAM, 2001.
- [35] M. KELLER, D. LENZ, AND R. K. WOJCIECHOWSKI, *Graphs and Discrete Dirichlet Spaces*, Grundlehren der mathematischen Wissenschaften, Springer, Cham, 2021.
- [36] E. KLANN AND R. RAMLAU, *Regularization by fractional filter methods and data smoothing*, Inverse Problems, 24 (2008), p. 025018.
- [37] A. LANZA, S. MORIGI, L. REICHEL, AND F. SGALLARI, *A generalized krylov subspace method for $\ell_p - \ell_q$ minimization*, SIAM Journal on Scientific Computing, 37 (2015), pp. S30–S50.
- [38] H. LI, J. SCHWAB, S. ANTHOLZER, AND M. HALTMEIER, *NETT: Solving inverse problems with deep neural networks*, Inverse Problems, 36 (2020), p. 065005.
- [39] Y. LOU, X. ZHANG, S. OSHER, AND A. BERTOZZI, *Image recovery via nonlocal operators*, Journal of Scientific Computing, 42 (2010), pp. 185–197.
- [40] T. R. MOEN, B. CHEN, D. R. HOLMES III, X. DUAN, Z. YU, L. YU, S. LENG, J. G. FLETCHER, AND C. H. MCCOLLOUGH, *Low-dose CT image and projection dataset*, Medical physics, 48 (2021), pp. 902–911.
- [41] E. MOROTTI, D. EVANGELISTA, AND E. LOLI PICCOLOMINI, *A green prospective for learned post-processing in sparse-view tomographic reconstruction*, Journal of Imaging, 7 (2021), p. 139.
- [42] E. MOROTTI, D. EVANGELISTA, AND E. L. PICCOLOMINI, *Increasing noise robustness of deep learning-based image processing with model-based approaches*, Numerical Computations: Theory and Algorithms NUMTA 2023, (2023), p. 155.
- [43] V. A. MOROZOV, *Methods for solving incorrectly posed problems*, Springer New York, NY, 1984.
- [44] S. MUKHERJEE, S. DITTMER, Z. SHUMAYLOV, S. LUNZ, O. ÖKTEM, AND C.-B. SCHÖNLIEB, *Learned Convex Regularizers for Inverse Problems*, 2020, <https://arxiv.org/abs/arXiv:2008.02839>.
- [45] G. PEYRÉ, S. BOUGLEUX, AND L. COHEN, *Non-local regularization of inverse problems*, in Computer Vision – ECCV 2008, D. Forsyth, P. Torr, and A. Zisserman, eds., Springer Berlin Heidelberg, 2008, pp. 57–68.
- [46] O. RONNEBERGER, P. FISCHER, AND T. BROX, *U-net: Convolutional networks for biomedical image segmentation*, in Medical Image Computing and Computer-Assisted Intervention–MICCAI 2015: 18th International Conference, Munich, Germany, October 5–9, 2015, Proceedings, Part III 18, Springer, 2015, pp. 234–241.
- [47] O. SCHERZER, M. GRASMAIR, H. GROSSAUER, M. HALTMEIER, AND F. LENZEN, *Variational methods in imaging*, Springer, 2009.
- [48] J. SCHWAB, S. ANTHOLZER, AND M. HALTMEIER, *Deep null space learning for inverse problems: convergence analysis and rates*, Inverse Problems, 35 (2019), p. 025008.
- [49] E. TJOA AND C. GUAN, *A survey on explainable artificial intelligence (xai): Toward medical xai*, IEEE transactions on neural networks and learning systems, 32 (2020), pp. 4793–4813.
- [50] Z. WANG, A. C. BOVIK, H. R. SHEIKH, AND E. P. SIMONCELLI, *Image quality assessment: from error visibility to structural similarity*, IEEE transactions on image processing, 13 (2004), pp. 600–612.
- [51] X. ZHANG, M. BURGER, X. BRESSON, AND S. OSHER, *Bregmanized nonlocal regularization for deconvolution and sparse reconstruction*, SIAM Journal on Imaging Sciences, 3 (2010), pp. 253–276.